

Real-Time Rainfall Estimation Using Satellite Signals: Development and Assessment of a New Procedure

Riccardo Angelo Giro^{ID}, Lorenzo Luini^{ID}, Senior Member, IEEE, Carlo Giuseppe Riva^{ID}, Senior Member, IEEE, Domingo Pimienta-del-Valle^{ID}, and José Manuel Riera Salis^{ID}, Senior Member, IEEE

Abstract—This contribution presents a comprehensive methodology for the real-time estimation of the rain intensity from downlink satellite signals. The enhanced system leverages on extremely randomized tree classifiers to automatically perform rainfall detection along earth–satellite links and successively employs an improved procedure to determine the corresponding slant-path rain attenuation. The latter quantity is then exploited to yield real-time rainfall rate estimates with a 1-min time resolution. The accuracy of the proposed methodology is tested using the *Ka*- and *Q*-band propagation data, collected in two different sites (Milan and Madrid) and in the framework of the propagation experiments. The results demonstrate the reliability of the automated rain event detector, as well as a satisfactory accuracy in estimating the slant-path rain attenuation and the point rainfall rate. The accuracy is assessed both on a statistical and on an instantaneous basis through the evaluation of different error figures and by inspection of individual time series.

Index Terms—Rainfall prediction, remote sensing, satellite communications, supervised machine learning, tropospheric effects.

I. INTRODUCTION

IN RECENT years, satellite communication systems operating at *Ka*-band and above have experienced an increased interest by operators and researchers [1]. Some of the latest technological developments, such as the deployment of the fifth-generation standard for cellular networks on a commercial scale, point toward a future evolution of mobile satellite systems, which will be likely integrated with fixed terrestrial networks [2]. However, the quality of earth-space communications operating at frequencies higher than 10 GHz, such as *Ka*-band, can be severely impaired by the effects induced by atmospheric constituents, such as hydrometeors, gases, and clouds: among these, the most relevant contribution to the attenuation at *Ka*- and *Q*-bands is given by rain [3]–[5].

In such a context, the knowledge of long-term rainfall statistics and (more importantly) of the instantaneous rain rate in a given location, assumes particular importance, since it

Manuscript received January 27, 2022; revised March 4, 2022; accepted March 27, 2022. Date of publication April 8, 2022; date of current version May 3, 2022. The Associate Editor coordinating the review process was Qiang Miao. (Corresponding author: Riccardo Angelo Giro.)

Riccardo Angelo Giro, Lorenzo Luini, and Carlo Giuseppe Riva are with the Dipartimento di Elettronica, Informazione e Bioingegneria, Politecnico di Milano, 20133 Milan, Italy (e-mail: riccardoangelo.giro@polimi.it).

Domingo Pimienta-del-Valle and José Manuel Riera Salis are with the Departamento de Señales, Sistemas y Radiocomunicaciones, Universidad Politécnica de Madrid, 28040 Madrid, Spain.

Digital Object Identifier 10.1109/TIM.2022.3165840

represents a fundamental requirement to apply fade mitigation techniques: for instance, high-throughput satellite systems make use of adaptive power control to ensure dynamic allocation of resources and guarantee the desired quality of service [6]. Among the different methodologies to estimate the rainfall intensity, the exploitation of earth-satellite links represents a real-time cheap and valuable solution, especially considering the high density of the receivers deployed worldwide [7]. As explained in [7] and [8], alternative methods or measurement instrumentation [9], [10] (e.g., networks of rain gauges, weather radars, microwave links, satellite infrared imagery, etc.) are each affected by technical drawbacks [11] which limit their context of application: for instance, rain gauges offer inadequate coverage over wide areas, whereas remote-sensing-based approaches are limited in spatial and temporal resolutions.

The approach presented here extends the methodology aimed at estimating rainfall rate using satellite signals [8] by proposing a real-time, fully operational implementation of such an approach, able to provide rain rate predictions with 1-min time resolution. The enhancements offered by the updated system include a data-driven rain event detector, able to automatically identify the presence of rain events along the earth-satellite link, and an improved procedure to estimate rain attenuation from the received satellite signal, which makes the rain rate prediction fully automated and thus applicable in real-time using any equipment receiving signals transmitted from a satellite operating at *Ku*-band or above. The methods currently available in [12]–[16] offer elaborate solutions either for the identification of rain events or for the estimation of the rainfall intensity from the received power, while the proposed model covers effectively both aspects: the identification of rain events is achieved by an accurate machine learning technique, and the rain rate prediction relies on a model underpinned by sound physical concepts (e.g., path reduction factors—accounting for the spatial inhomogeneity of precipitation along the link, the dependence of the rain height on the season, and the different impact of stratiform and convective events [8]). Finally, while the other methods are devised and tested using quite limited datasets (mostly collected in a single site), the proposed model is tested against a full year of measurements and its performance appears to be independent of frequency and site, as shown by the tests performed on two distinct geographical locations (Milan, Italy, and Madrid, Spain) and at different operational frequencies

(*Ka*- and *Q*-bands). All these features offer a reliable, accurate, and robust real-time method for the prediction of rain rates from satellite signals.

The remainder of this article is organized as follows. Section II describes the experimental setup and datasets used in this work, followed by the data processing and preparation phases. Section III presents the characteristics of the proposed real-time rainfall estimation method. Section IV is devoted to assessing system performance and reliability. Finally, Section V draws some conclusions.

II. EXPERIMENTAL SETUP, DATASETS, AND DATA PREPROCESSING

A. Experimental Setup and Datasets

The data used in this work have been collected for an entire year in the framework of the Alphasat Aldo Paraboni propagation experiment [17], from January 1 to December 31 2017. The Alphasat propagation payload is composed of two continuous-wave coherent beacon transmitters at 19.701 GHz (*Ka*-band) and 39.402 GHz (*Q*-band), with frequency stability of 3 parts per million (ppm). The payload includes standard *Ka*-band beacon transmitters, *Q*-band solid-state power amplifiers, a *Ka*-band low-pass filter, and two separate horn antennas for *Ka*- and *Q*-bands. The effective isotropic radiated power is about 19.9 and 26.8 dBW at *Ka*- and *Q*-bands, respectively [18].

The experimental measurements have been obtained from the instrumentation installed at Politecnico di Milano, Milan [19] (latitude 45.48°N, longitude 9.23°E, and an altitude above the mean sea level of 137 m) and at Universidad Politécnica de Madrid, Madrid (40.45°N, 3.73°W, and an altitude above mean sea level of 680 m).

The equipment located in Milan consists in: two beacon receivers (*Ka*-band at 19.701 GHz and *Q*-band at 39.402 GHz), each recording at 8 Hz the power levels of *Ka*- and *Q*-band signals transmitted by the Alphasat satellite (geostationary orbit at 25°E); a Thies Clima Laser Precipitation Monitor, which is an optical disdrometer providing point rain rate measurements with a sampling interval of 1 min. The instrumentation installed in Madrid, instead, comprises a *Ka*-band beacon receiver, which captures the signal from the geostationary satellite KA-SAT (located at 9°E, frequency of 19.68 GHz, EIRP equal to 15 dBW) and a Thies Clima optical disdrometer and rain gauge for rainfall rate measuring with 1-min integration time. The *Ka*-band receiver is reused from a previous experiment and is described in [20]. The experimental datasets employed in this work are summarized in Table I. They include all the physical quantities previously mentioned and are completed, both for Milan and Madrid, by: 0° isotherm height time series, extracted every hour from vertical temperature profiles provided by the European Centre for Medium-Range Weather Forecasts (ECMWF); *Ka*-band rain attenuation time series, manually derived from the power levels recorded by the *Ka*-band beacon receivers (using the well-established procedure described in [21]).

TABLE I
EXPERIMENTAL DATASETS

Location	Physical quantity	Units	Sampling rate	Samples
Milan	Received power (Ka band)	dBm	8 Hz	252288000
	Received power (Q band)	dBm	8 Hz	252288000
	Rain attenuation	dB	8 Hz	252288000
	Rain rate	mm/h	1 sample/min	525600
Madrid	Zero-degree isotherm height	km	1 sample/h	8760
	Received power (Ka band)	dBm	18.78 Hz	592246080
	Rain attenuation	dB	18.78 Hz	592246080
	Rain rate	mm/h	1 sample/min	525600
	Zero-degree isotherm height	km	1 sample/h	8760

B. Data Preprocessing

This section illustrates how to process the raw data listed in Table I, which are required as input to the automated rain event detector and to the rainfall estimation procedure presented in [8]. As previously discussed in Section II-A, such signals originate from different domains, so they need to be standardized before being effectively employable in the aforementioned algorithms: this results in a set of common operations to be performed for each of these physical quantities. In addition, certain elements of the dataset require dedicated processing for different reasons, each of which will be clarified later on in this section.

First, it is necessary to unify all the data to the same sampling rate. Since the goal is to provide rain rate estimates with a 1-min time resolution, it was decided to resample all the signals with a measurement frequency f_s of 1 sample/min: as a result, the received power and measured attenuation time series collected in Milan have been averaged over non-overlapping windows of 480 samples; similarly, the size of the averaging window employed to decimate Madrid's propagation data is equal to 1127 samples. Reducing the sampling rate also allows to filter out atmospheric scintillations, which produce undesired, rapid amplitude variations on the received power and rain attenuation time series [21], [8]: as a matter of fact, this operation can be seen as a low-pass filter applied to each of the aforementioned signals with a cutoff frequency of approximately 0.008 Hz (the bandwidth B of a signal sampled at frequency f_s is equal to $f_s/2$, thus $B = 1/(2 \times 60) \approx 0.008$ Hz), a value within the range (0.001–1 Hz) recommended by the International Telecommunication Union – Radiocommunication Sector (ITU-R) [22].

The isotherm height values, instead, have been oversampled by an integer factor equal to 60. As a result, each of the quantities listed in Table I can therefore be seen as an $m \times 1$ column vector, where $m = 525\,600$.

Another element of disturbance that degrades the quality of received power signals is represented by low-frequency amplitude fluctuations due to day/night temperature variations affecting the gain of the beacon receiver chain. The magnitude of such oscillations can reach up to 20% of the average signal level and needs to be removed for the proper automatic identification of rain events. For this reason, we have decided to generate high-pass versions of the previously filtered power

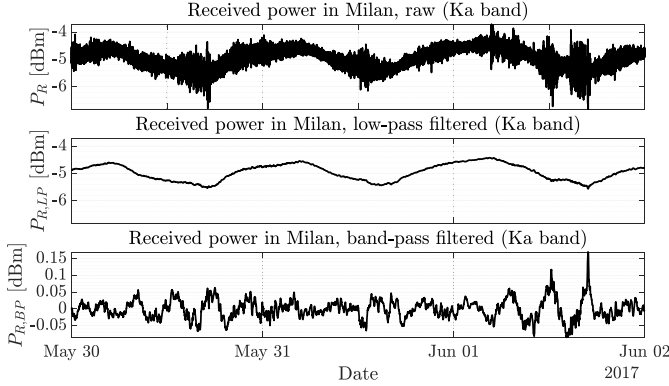


Fig. 1. Raw (top), low-pass (middle), and bandpass (bottom) filtered versions of the received power in Milan (*Ka*-band), between May 30, 2017, and June 2, 2017.

time series and those will be employed in the data-driven rain event detector. We have therefore applied a causal high-pass finite impulse response (FIR) filter, designed using a Kaiser window. The filter is characterized by 8315 coefficients, a stop-band attenuation of 60 dB and a passband ripple of 0.1 dB. The cutoff frequency has been set to approximately $46.3 \mu\text{Hz}$, thus attenuating signal components having a period longer than 6 h. As an example, Fig. 1 shows the trend of received power in Milan between May 30 and June 2, 2017 (*Ka*-band). The topmost plot represents the raw received power signal, the middle one corresponds to its low-pass version ($P_{R,LP}$, which will be used to estimate rain attenuation), whereas the bottom one ($P_{R,BP}$, given as input to the rain detector) is equivalent to a bandpass filtered version of the original power signal, having passband frequency range between $46.3 \mu\text{Hz}$ and 0.008 Hz .

Last, one needs to rule out, for each of the two locations, all the instances in which at least a piece of equipment was not operational or provided faulty measurements (e.g., due to power supply failures). This resulted in a size reduction of each processed signal from $m = 525\,600$ to $m = 409\,943$ (Milan) and $m = 513\,369$ (Madrid) samples, respectively.

As further explained in Section III-B, the real-time rainfall estimation method proposed in this work includes an intermediate step devoted to deriving the rain attenuation A_R from the received signal. On the other hand, A_R can also be obtained by using the customary approach explained in [21]: when there is no need for real-time estimates, the received beacon power P_R is first low-pass-filtered to remove scintillations (e.g., obtaining a signal similar to $P_{R,LP}$) and afterward rain events are identified, usually both by taking advantage of the local rain sensors and by inspecting the trend of $P_{R,LP}$: indeed, the impact of rain on the link might be longer than what is recorded by the disdrometer, especially at the beginning and/or the end of the event. Finally, A_R is calculated by subtracting from $P_{R,LP}$ the power level or baseline level that is estimated as the linear interpolation of $P_{R,LP}$ from just before the beginning to just after the end of each event. The A_R data obtained by means of this approach, hereinafter to be referred to as “measured rain attenuation,” will be used as the reference to assess the accuracy of the A_R values obtained using the real-time approach proposed in this work.

III. REAL-TIME RAINFALL ESTIMATION METHOD

As stated in Section I, the primary goal of this research consists in developing an automated procedure to detect in real-time the presence of rain events in a given location and, in the affirmative case, determine the intensity of the precipitation. The entire estimation procedure consists of three main steps, which are thoroughly described in this section: rain event detection, rain attenuation assessment, and rain rate estimation.

A. Data-Driven Rain Event Detector

To perform the detection task, we have trained an extremely randomized trees classifier (ERTC) [23], which is a supervised, data-driven meta-estimator able to automatically assess the presence of rain by analyzing in real-time certain characteristics (features) of a given input signal, such as the one reported in Fig. 1 (bottom). ERTCs share the same working principle of standard decision tree classifiers (DTCs), in which a machine is trained to predict two or more discrete categories (e.g., rain/no rain) based on a set of simple and intuitive decision rules [24], which are directly derived from the input features.

Implementing an ERTC can be more advantageous, compared to a DTC, for a number of reasons. First of all, ERTCs do not exhibit the high-variance issues affecting DTCs [25], which are usually associated to overfitting a model to the data: in ERTCs, the variance is in fact reduced by averaging the estimates provided by several DTCs; second, they do not favor features having high cardinality (namely, with several unique values) [26], which may become problematic when computing statistical indicators from continuous random variables; last, they also provide information, by means of relative rank assessment, on which features contribute the most to the final prediction [26].

We summarize here the main parameters of the ERTC, along with the corresponding values chosen in this work.

1) *Number of estimators*, $n_{\text{trees}} = 100$: It determines the number of trees in the random forest. Larger values of this quantity (e.g., >25) increase the accuracy of the algorithm (e.g., greater averaging power), at the expense of increased computational times. It should be noted that the performance gain tends to saturate after a certain threshold (e.g., >100) and therefore the results do not improve significantly.

2) *Criterion split*: It defines the rule employed to measure the quality of a tree node split. We have chosen Gini impurity [27], which measures the likelihood of misclassifying an observation of a random process.

3) *Maximum number of features*, $N_{\text{max}} = 68$: It corresponds to the number of random features to consider when splitting each tree node. Lower values lead to a model with high bias and more robustness to variance; increasing N_{max} allows the ERTC to choose among a larger pool of the best features to evaluate at each node split.

As mentioned at the beginning of Section III-A, the proposed rain event detector belongs to the category of supervised binary classifiers, so it requires as input a vector of reference truth labels, y : the latter corresponds to a set of manually tagged instances indicating the true class to be predicted

(e.g., rain/no rain). Categorical labels, such as the ones considered here, can be numerically represented by means of one-hot encoding: being $y[k]$ the k th value of \mathbf{y} , one can set $y[k] = 1$ in the case of rain and $y[k] = 0$ otherwise. To perform such a task, we have made use of the available rain attenuation measurements \mathbf{A}_R : rain is said to occur whenever any given value $A_R[k]$ of vector \mathbf{A}_R is higher than zero. This condition can be formally expressed as

$$y[k] = \begin{cases} 1, & A_R[k] > 0 \\ 0, & A_R[k] = 0. \end{cases} \quad (1)$$

The above-mentioned process was executed to derive two vectors of reference truth labels, one for the site of Milan and another for that of Madrid.

Besides a target vector \mathbf{y} , the rain event detector requires an $m \times N$ feature matrix \mathbf{X} as input, where N corresponds to the number of evaluated features. Such a matrix encompasses a set of statistical indicators, computed from the bandpass versions of the received power signals described in Section II-B: to this purpose, we have evaluated four moving statistics (mean, standard deviation, minimum, and maximum), each over 17 different and causal time windows ranging from 5 min up to 6 h. Such timeframes have been carefully designed to include various intervals encompassing different types of rain events (e.g., sudden storms, long and light rainfall, etc.). The upper bound has been set to 6 h because, as seen in the preprocessing part of Section II-B, signal components having a period longer than 6 h have been removed by means of a high-pass filter. The lower bound, instead, was determined as a tradeoff between the temporal resolution of the available measurements and a reasonably large enough time window to evaluate the selected statistics.

As a result, each input power sample $x[k]$ is transformed into a row feature vector \mathbf{x}_k having dimensions equal to $1 \times N$, where $N = 68$. Moreover, the feature matrix is standardized using Z-score normalization, where each column of \mathbf{X} is transformed to remove its mean value and have unit variance. Considering an $m \times N$ feature matrix \mathbf{X} , the normalized $m \times 1$ vector \mathbf{x}'_n corresponding to the n th feature is computed as

$$\mathbf{x}'_n = \frac{1}{\sigma_n}(\mathbf{x}_n - \mu_n) \quad (2)$$

where the $m \times 1$ vector \mathbf{x}_n refers to the n th column of \mathbf{X} , characterized by mean μ_n , and has variance equal to σ_n .

Last, the process of feature evaluation and normalization is repeated both for the *Ka*- and *Q*-band power signals collected in Milan and for the *Ka*-band data measured in Madrid, ultimately attaining three distinct feature matrices.

The ERTC was trained using 80% of the available *Q*-band data. It has instead been tested with the remaining 20%, together with the entire *Ka*-band datasets (Milan and Madrid). An example of the real-time output provided every minute by the binary classifier is displayed in Fig. 2: the labels predicted for a rain event that occurred on June 28, 2017, using Milan, the *Ka*-band data (lowermost plot) can be visually compared to the true values (middle plot), which have been directly obtained from the available rain attenuation

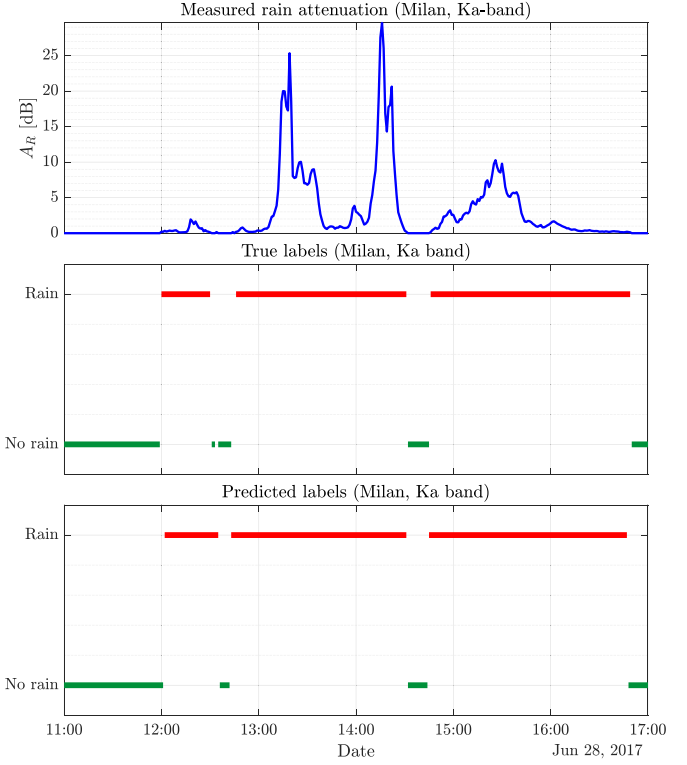


Fig. 2. From top to bottom: measured *Ka*-band rain attenuation, true labels, and predicted labels on June 28, 2017, in Milan, using the *Ka*-band data.

measurements (blue curve on the topmost graph) by manual inspection.

B. Rain Attenuation Estimation

Once rain events are identified using the algorithm discussed in Section III-A, slant-path rain attenuation can be estimated by evaluating the difference between a fixed quantity $\hat{P}_{R,\text{LP}}$ and the low-pass version of the received power signal, $P_{R,\text{LP}}$. $\hat{P}_{R,\text{LP}}$ corresponds to the baseline level of $P_{R,\text{LP}}$ in clear sky conditions, namely in the absence of rain; it is defined as the mean value of $P_{R,\text{LP}}$, computed over a time window of K minutes before the beginning of a rain event occurring at a particular time \bar{k}

$$\hat{P}_{R,\text{LP}} = \frac{1}{K} \sum_{i=1}^K P_{R,\text{LP}}[\bar{k} - i] \text{ [dBm].} \quad (3)$$

After deriving $\hat{P}_{R,\text{LP}}$ for a specific event, the instantaneous rain attenuation $\hat{A}_R[k]$ for that event can be estimated as

$$\hat{A}_R[k] = \hat{P}_{R,\text{LP}} - P_{R,\text{LP}}[k] \text{ [dB].} \quad (4)$$

To determine the best value of K , we have investigated the trend of the root mean square (RMS) value of the estimation error ϵ_{A_R} , defined as the difference between \hat{A}_R and the available rain attenuation measurements A_R , as a function of K . Such an operation, performed for the site of Milan, is displayed in Fig. 3, where $\text{RMS}\{\epsilon_{A_R}\}$ is plotted as a function of the window length K . We have opted for $K = 8$ as the first value guaranteeing the following: first, it is desirable to minimize the RMS value of the estimation error; second, the

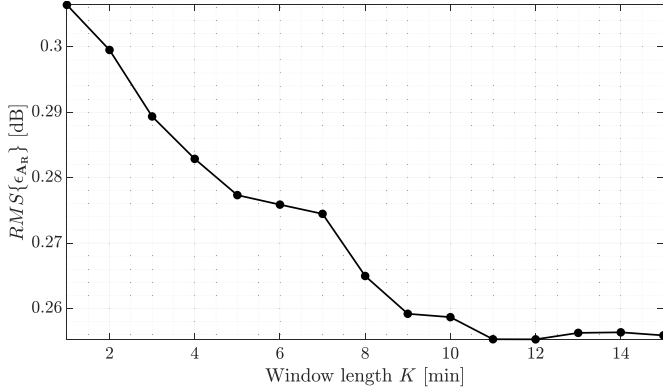


Fig. 3. RMS values of the error ϵ_{A_R} on the estimated rain attenuation, as a function of the window length K , for the site of Milan (dotted line).

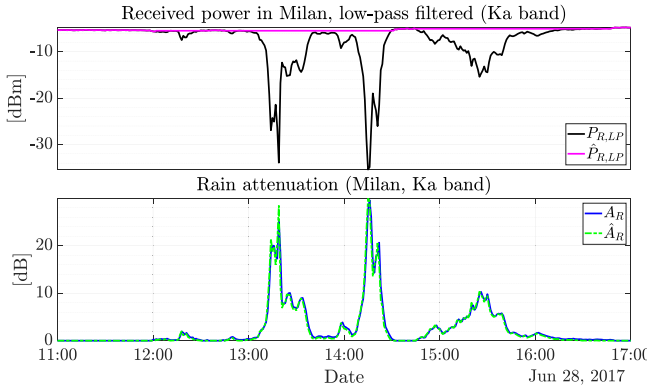


Fig. 4. From top to bottom: received power (black line), estimated baseline (magenta line), measured (blue line), and estimated (green line) rain attenuation on June 28, 2017, in Milan (Ka-band).

time window cannot be too small (e.g., <5 min), otherwise $\hat{P}_{R,LP}$ would be susceptible to short-term signal variations; last, larger values of K should be avoided (e.g., >10 min), since certain types of rain events (e.g., convective) can occur in rapid succession and require a quick estimation of the baseline power level. Although the values of $K = 9$ and 10 provide a marginally lower RMS value (compared to $K = 8$), they do not offer a significant gain (less than 0.01 dB) and they are progressively closer to the upper bound of 10 min, which is not desirable.

As an example, Fig. 4 displays the trend of the received power (Ka-band) in Milan on June 28, 2017 (topmost plot, black line), along with the estimated baseline level $\hat{P}_{R,LP}$ (magenta line). The bottom graph depicts the temporal evolution of the measured (blue line) and of the estimated (green line) rain attenuation. The entire estimation process proves to be satisfactory both from a statistical (low $\text{RMS}\{\epsilon_{A_R}\}$) and an instantaneous point of view (good agreement of the curves for individual events).

Last, once rain attenuation is estimated, the rain rate can be computed using the procedure described in [8].

C. Full Procedure for Real-Time Prediction of the Rain Rate

This section summarizes the full procedure for the real-time prediction of the rain rate, which is applied only to the Ka-band data. Indeed, the dynamic range of the Q -band

receiver in Milan is around 35 dB, which limits the rain rate retrieval roughly to 50 mm/h; on the contrary, at Ka-band, using the same dynamic range, rain rates higher than 100 mm/h can be estimated [8]. Based on these results, it is recommended to exploit satellite signals at Ka-band: not only they are much more available nowadays (if compared to higher frequency bands), but, in addition, the same receiver dynamic range will obviously allow increasing the maximum rain rate value that can be measured; finally, at Q - and V -bands, cloud attenuation increases as well, which might affect to some extent the rain rate retrieval.

The full procedure to estimate the rain rate consists in the following steps:

- 1) measure the instantaneous received beacon power, $P_{R,LP}[k]$;
- 2) using the bandpass-filtered power $P_{R,BP}[k]$, compute the corresponding feature vector x and standardize it using Z-score normalization;
- 3) evaluate the output $\hat{y}[k]$ provided by feeding the ERTC with x as input;
- 4) if $\hat{y}[k] = 0$,
 - a) $\hat{P}_{R,LP} = P_{R,LP}[k]$;
else if $\hat{y}[k] = 1$ and $\hat{y}[k - 1] = 0$,
 - b) Compute the baseline level $\hat{P}_{R,LP}$ using (3);
Otherwise,
 - c) A rain event is occurring and $\hat{P}_{R,LP}$ has already been computed at a previous time step;
- 5) Estimate $\hat{A}_R[k]$ using $\hat{P}_{R,LP}$ and the low-pass filtered power $P_{R,LP}[k]$ in (4);
- 6) If $\hat{A}_R[k] > 0$,
 - d) Obtain the value of the 0° isotherm height at time k , $h[k]$;
 - e) Estimate $\hat{R}[k]$ providing $\hat{A}_R[k]$ and $h[k]$ as input to the algorithm described in [8];
- Otherwise,
- f) $\hat{R}[k] = 0$.

Step 6) above relies on the inversion model proposed in [8], to which the reader is addressed for more details. Here, it will suffice to briefly recall that such a methodology aims at estimating the point rain rate from the rain attenuation affecting an earth-space path by using a closed-form analytical expression derived from the inversion of the rain attenuation model adopted by the ITU-R in recommendation P.618-13 [28]. The prediction model also accounts for the diverse effects of stratiform and convective events on the link: the former, typically of limited intensity and long duration, is associated with the presence of the bright band, which is accounted for through an additional equivalent rain height; the latter, much more intense and localized in space and time, shows a much higher rain height (due to convective updrafts and downdrafts pushing hydrometeors well above the 0°C isotherm height), modeled by means of a rain height enhancement factor, in turn dependent on the local convectivity ratio β [8].

TABLE II
PERFORMANCE OF THE RAIN EVENT DETECTOR
(EXPRESSED IN PERCENTAGE)

Instance	Test set	Samples	\mathcal{P}	\mathcal{R}	\mathcal{F}_1
No rain	Q band, Milan	70729	99.60%	99.78%	99.69%
	Ka band, Milan	383054	99.51%	99.73%	99.62%
	Ka band, Madrid	488304	99.55%	99.70%	99.62%
Rain	Q band, Milan	7498	97.86%	96.23%	97.03%
	Ka band, Milan	26889	96.04%	93.02%	94.50%
	Ka band, Madrid	25065	94.01%	91.16%	92.56%

IV. PERFORMANCE EVALUATION

A. Prediction Accuracy of the ERTC

To assess the prediction accuracy of the rain event detector, we consider the typical metrics used in statistical analysis of binary classification, which correspond to precision \mathcal{P} , recall \mathcal{R} , and \mathcal{F}_1 score [29], [30]. Such indicators all range between 0 and 1; an ideal estimator achieves a score equal to 1 for each one of those quantities, which are, respectively, defined as

$$\mathcal{P} = \frac{T_p}{T_p + F_p} \quad (5)$$

$$\mathcal{R} = \frac{T_p}{T_p + F_n} \quad (6)$$

$$\mathcal{F}_1 = 2 \frac{\mathcal{P}\mathcal{R}}{\mathcal{P} + \mathcal{R}} \quad (7)$$

where T_p , F_p , and F_n are the number of true positives, false positives, and false negatives, respectively, computed by comparing the output \hat{y} provided by the ERTC with the ground-truth labels y . Table II reports the results obtained using three different test sets, which correspond to the *Q*- and *Ka*-band data collected in Milan, along with the *Ka*-band measurements obtained in Madrid. This threefold subdivision has multiple purposes: first, evaluate the model capabilities on data belonging to the same distribution of the training set (*Q*-band, Milan); successively, test measurements collected at a different frequency (*Ka*-band, Milan); finally, introduce also a change in the geographical location (*Ka*-band, Madrid). For a more comprehensive comparison, it was decided to assess separately the classification performance achieved on the two cases “rain” and “no rain,” since the latter class contains a much larger number of samples (with respect to the former) and is an easier instance to be correctly detected, so it might hinder the true results.

As it can be observed from Table II, the performance of the ERTC proves to be satisfactory, as the overall prediction accuracy is above 91% for all the instances and metrics considered.

B. Comparison of the ERTC With Other Models

After verifying the reliability of the ERTC in detecting rain events, it is useful to compare its performance against other supervised classifiers. The literature is very prolific in this sense, as there are many machine learning algorithms

TABLE III
COMPARISON OF DIFFERENT MODELS ON THE *Q*-BAND
MILAN DATASET, NO RAIN CLASS

Instance	Test set	Samples	Model	\mathcal{P}	\mathcal{R}	\mathcal{F}_1
No rain	Q band, Milan	70729	ERTC	99.60%	99.78%	99.69%
			DTC	94.36%	98.10%	96.19%
			RFC	94.90%	99.17%	96.99%
			ADA	94.51%	99.17%	96.78%
			KNN	94.75%	98.43%	96.55%
			QDA	94.90%	98.87%	96.85%
			SVM	95.96%	97.09%	96.52%

available, offering very basic solutions, as well as much more complex ones, such deep neural networks; including them all would go beyond the scope of this work, and therefore we have restricted our choice to a subset. We recall that our main research goal is to propose a complete rainfall estimation procedure that can be easily deployed on low-cost processing architectures, and therefore the candidate rain detection algorithms must concurrently satisfy the following requirements:

- 1) Ease of implementation.
- 2) Low computational complexity.

Following this choice, we have compared the ERTC with its two closest counterparts, namely the DTC [24] and the random forest classifier (RFC) [26], along with other solutions, such as: the AdaBoost (ADA) algorithm [31]; k-nearest neighbors (KNNs) [32]; quadratic discriminant analysis (QDA) [33]; and support vector machines (SVMs) [34]. For each instance and test set reported in Table II, we have evaluated the values of \mathcal{P} , \mathcal{R} , and \mathcal{F}_1 , resulting thus in a set of six different tables (see Tables III–VIII). Moreover, we have highlighted in every table the maximum value achieved in the three aforementioned metrics, along with the best model in a given combination of instance and test set: recalling that \mathcal{F}_1 is a function of both \mathcal{P} and \mathcal{R} , a model is declared as a winner whenever its \mathcal{F}_1 score is greater than all the other candidates. As it can be inferred from Tables III–V, the performance in correctly predicting the no rain class is fairly similar across all models and test sets. Significant discrepancies instead occur during the rain detection instance (e.g., Tables VI–VIII), and it becomes clear that in such circumstances all the models but the ERTC fail to generalize well enough and show unequivocal signs of overfitting to *Q*-band, the Milan training set.

C. Estimation Accuracy of the Rain Attenuation

As a third step, it is necessary to assess the reliability of the rain attenuation estimation obtained by adopting the procedure described in Section III-B. To this aim, we have evaluated the mean E , standard deviation σ , and RMS values of ϵ_{A_R} for both locations, using a window length K equal to 8 min. The results are reported in Table IX and reveal, in both cases, an approximately unbiased estimation error with an RMS value of 0.265 and 0.273 dB, respectively, for Milan and Madrid.

TABLE IV
COMPARISON OF DIFFERENT MODELS ON THE *Ka*-BAND
MILAN DATASET, NO RAIN CLASS

Instance	Test set	Samples	Model	\mathcal{P}	\mathcal{R}	\mathcal{F}_1
No rain	Ka band, Milan	383054	ERTC	99.51%	99.73%	99.62%
			DTC	97.72%	94.88%	96.28%
			RFC	98.20%	97.86%	98.03%
			ADA	97.84%	97.61%	97.72%
			KNN	97.84%	95.18%	96.49%
			QDA	98.79%	92.48%	95.53%
			SVM	98.92%	91.69%	95.16%

TABLE V
COMPARISON OF DIFFERENT MODELS ON THE *Ka*-BAND
MADRID DATASET, NO RAIN CLASS

Instance	Test set	Samples	Model	\mathcal{P}	\mathcal{R}	\mathcal{F}_1
No rain	Ka band, Madrid	488304	ERTC	99.55%	99.70%	99.62%
			DTC	98.13%	84.58%	90.85%
			RFC	98.54%	94.08%	96.26%
			ADA	98.23%	94.07%	96.10%
			KNN	98.22%	88.68%	93.21%
			QDA	99.58%	67.12%	80.19%
			SVM	98.61%	76.04%	85.86%

TABLE VI
COMPARISON OF DIFFERENT MODELS ON THE *Q*-BAND
MILAN DATASET, RAIN CLASS

Instance	Test set	Samples	Model	\mathcal{P}	\mathcal{R}	\mathcal{F}_1
Rain	Q band, Milan	7498	ERTC	97.86%	96.23%	97.03%
			DTC	84.40%	63.64%	72.56%
			RFC	92.89%	66.94%	77.81%
			ADA	92.55%	64.31%	75.89%
			KNN	87.15%	66.20%	75.24%
			QDA	90.54%	67.08%	77.07%
			SVM	80.51%	74.64%	77.46%

TABLE VII
COMPARISON OF DIFFERENT MODELS ON THE
Ka-BAND MILAN DATASET, RAIN CLASS

Instance	Test set	Samples	Model	\mathcal{P}	\mathcal{R}	\mathcal{F}_1
Rain	Ka band, Milan	26889	ERTC	96.04%	93.02%	94.50%
			DTC	48.40%	68.41%	56.69%
			RFC	70.90%	74.39%	72.60%
			ADA	67.01%	69.27%	68.12%
			KNN	50.53%	70.11%	58.73%
			QDA	43.91%	83.81%	57.63%
			SVM	41.98%	85.70%	56.36%

D. Estimation Accuracy of the Rain Rate

Last, it is worth verifying the accuracy of rain rate predictions obtained using $\hat{\mathbf{A}}_R$ (*Ka*-band) as input to the method

TABLE VIII
COMPARISON OF DIFFERENT MODELS ON THE
Ka-BAND MADRID DATASET, RAIN CLASS

Instance	Test set	Samples	Model	\mathcal{P}	\mathcal{R}	\mathcal{F}_1
Rain	Ka band, Madrid	25065	ERTC	94.01%	91.16%	92.56%
			DTC	18.59%	68.57%	29.25%
			RFC	38.70%	72.85%	50.55%
			ADA	36.69%	66.99%	47.41%
			KNN	23.74%	68.63%	35.27%
			QDA	12.85%	94.43%	22.62%
			SVM	14.49%	79.09%	24.49%

TABLE IX
ESTIMATION ERROR ON RAIN ATTENUATION

Frequency band, location	$E\{\epsilon_{A_R}\}$ [dB]	$\sigma\{\epsilon_{A_R}\}$ [dB]	$RMS\{\epsilon_{A_R}\}$ [dB]
Ka band, Milan	-0.094	0.248	0.265
Ka band, Madrid	-0.046	0.269	0.273

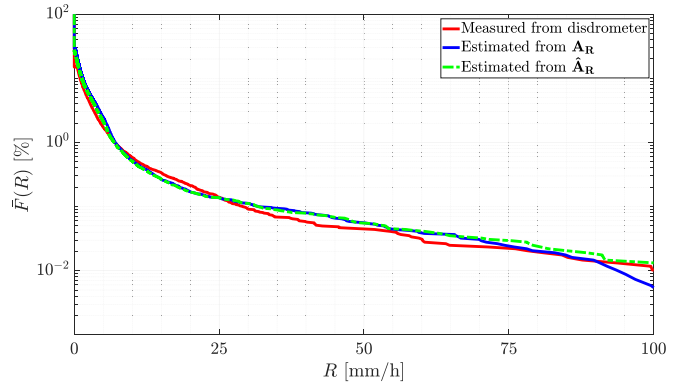


Fig. 5. Annual rain rate CCDF for Milan (predictions using the *Ka*-band data).

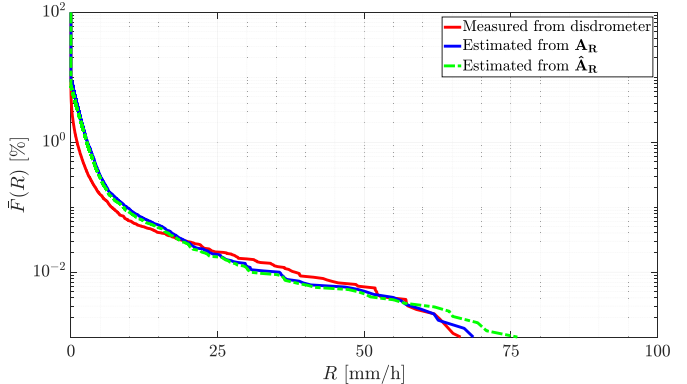


Fig. 6. Annual rain rate CCDF for Madrid (predictions using the *Ka*-band data).

discussed in [8] and recalled in Section III-C, both from a statistical and an instantaneous point of view (time series). The estimated rain rate will be compared with that measured by the disdrometer.

We have evaluated, for both sites, the annual complementary cumulative distribution functions (CCDFs) of rain rate $\bar{F}(R)$, which are displayed in Figs. 5 (Milan) and

TABLE X
ESTIMATION ERROR STATISTICS FOR ALL RAIN EVENTS
OCCURRED IN MILAN IN 2017

Input attenuation	$E\{\epsilon_{R_T}\}$ [mm]	$RMS\{\epsilon_{R_T}\}$ [mm]	$E\{\epsilon_{R_M}\}$ [mm/h]	$RMS\{\epsilon_{R_M}\}$ [mm/h]	$E\{\epsilon_{\bar{R}}\}$ [mm/h]	$RMS\{\epsilon_{\bar{R}}\}$ [mm/h]
\hat{A}_R	1.12	6.17	-1.97	14.75	-0.87	3.19
A_R	1.39	5.34	-2.15	11.83	0.04	1.52

TABLE XI
ESTIMATION ERROR STATISTICS FOR ALL RAIN EVENTS
OCCURRED IN MADRID IN 2017

Input attenuation	$E\{\epsilon_{R_T}\}$ [mm]	$RMS\{\epsilon_{R_T}\}$ [mm]	$E\{\epsilon_{R_M}\}$ [mm/h]	$RMS\{\epsilon_{R_M}\}$ [mm/h]	$E\{\epsilon_{\bar{R}}\}$ [mm/h]	$RMS\{\epsilon_{\bar{R}}\}$ [mm/h]
\hat{A}_R	1.18	5.57	0.53	21.95	0.72	1.32
A_R	1.44	6.04	-0.55	10.29	0.75	1.31

6 (Madrid). We have also considered, for every event, the mean E and RMS values of the estimation errors ϵ_{R_T} , ϵ_{R_M} , and $\epsilon_{\bar{R}}$, respectively, calculated on the total accumulated rainfall R_T , maximum rain rate R_M , and mean rain rate \bar{R} : all the aforementioned error figures are defined as the difference between the estimates and the measurements obtained from the disdrometer. Tables X and XI report the mean and RMS values of such errors, respectively, corresponding to the locations of Milan and Madrid. The results obtained so far are quite satisfactory, as the annual CCDFs of the estimates obtained from \hat{A}_R (green lines) show good agreement with the ones obtained from A_R (blue curves) and with the reference measurements (red lines). In addition, the error figures obtained when using \hat{A}_R as input to the rain rate prediction model presented in [8] are very similar to the results previously obtained by employing A_R . This level of consistency is verified in both sites and is additionally confirmed when inspecting the trend of individual time series: as a reference, Figs. 7 and 8 show the evolution of the rain rate [see Fig. 7 (top)] and accumulated rainfall [see Fig. 7 (bottom)] in Milan on September 10, 2017, and in Madrid on July 7, 2017, respectively. In both cases, the rain rate predictions produced by the new estimation procedure (green curves) are in line with the previous results (blue curves) and are typically in advance of few minutes with respect to the measurements (red lines). The latter aspect becomes particularly advantageous when exploiting rain rate predictions to promptly raise early alerts of incoming rainstorms. Indeed, though the proposed rain rate estimation model predicts the point rain rate at the receiver site (as it includes path reduction factors to consider the spatial distribution of the rain rate along the path [8]), any rain attenuation value affecting the link (i.e., any precipitation along the path) will produce a rain estimate. Point rainfall rain sensors (e.g., disdrometer), instead, provide information only on the precipitation affecting a specific site. The estimation accuracy reported in Tables X and XI for Milan and Madrid is similar, which seems to indicate that the method does not present performance differences for the climates the two sites are subject to. Finally, comparison of Fig. 7 (reporting an event lasting almost a full day) and Fig. 8 (showing shorter events) suggests that the estimation accuracy of the proposed model

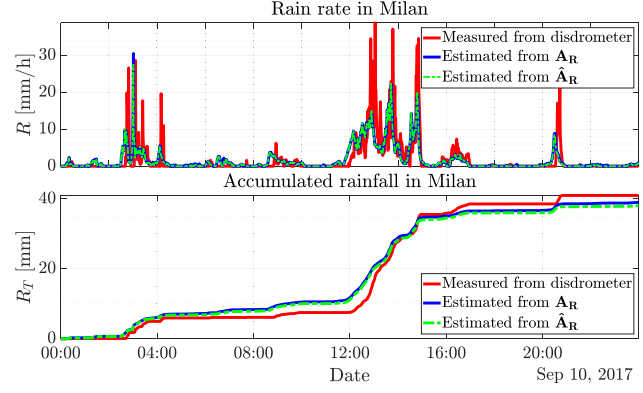


Fig. 7. Rain rate (top) and accumulated rainfall (bottom) in Milan on September 10, 2017.

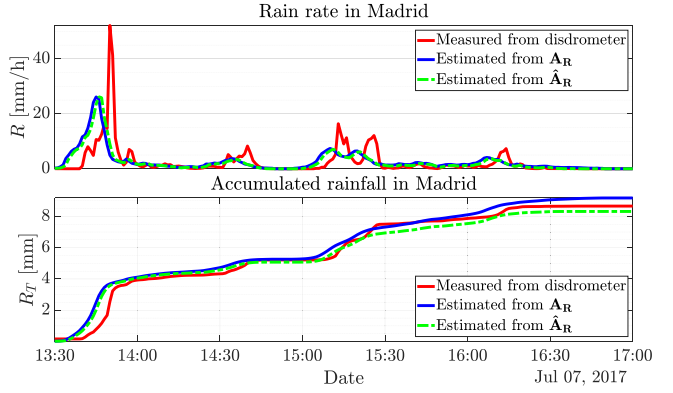


Fig. 8. Rain rate (top) and accumulated rainfall (bottom) in Madrid on July 7, 2017.

does not depend on the duration of the precipitation: in both cases (and in several others not reported here in detail for the sake of brevity), the predicted accumulated rainfall is in good agreement with the one measured by the disdrometer.

V. CONCLUSION

This contribution presented several enhancements to the rainfall rate estimation algorithm presented in [8]: more specifically, we proposed a fully operational implementation of such procedure, able to provide real-time rain rate predictions with 1-min time resolution. The upgraded system allows to automatically detect the presence of rain events along earth-satellite links and to accurately estimate the level of rain attenuation from the received beacon signal, hence of the point rain rate.

The enhanced model was tested using the *Ka*-band propagation data collected in Milan and Madrid in the framework of propagation experiments: though also *Q*-band data are available at both sites, the latter would obviously lead to a lower maximum retrievable rain rate value, due to the higher attenuation levels and to the limited dynamic range of the receiver. Overall, it is recommended to apply the proposed model taking advantage of satellite signals at *Ka*-band, not only because they are widely available nowadays, but also because they are less affected by cloud attenuation (if compared to higher frequency bands), which might decrease to some extent the rain rate retrieval accuracy.

The outputs provided by the automated rain rate predictor were compared to reference measurements provided by locally installed disdrometers. The results obtained so far confirm a solid reliability in the identification of rain events, achieving a detection accuracy higher than 91% for all the metrics considered. The proposed procedure, which automatically extracts rain attenuation from the received power signal, also proved to be satisfactory, achieving values of $\text{RMS}\{\epsilon_{A_k}\}$ equal to 0.265 and 0.273 dB at *Ka*-band, respectively, for the locations of Milan and Madrid. The accuracy of the rain rate predictions was comparable with the results attained from the model in [8], as the currently achieved values of $\text{RMS}\{\epsilon_{\bar{R}}\}$ are equal to 3.19 mm/h (Milan) and 1.32 (Madrid) mm/h, whereas $\text{RMS}\{\epsilon_{R_T}\}$ is 6.17 mm/h (Milan) and 5.57 (Madrid) mm/h. Similarly, the manual inspection of individual time series revealed good agreement between predictions and the available measurements.

Future work will be focused on exploiting the model presented in this work to implement a system able to perform accurate large-scale measurements of the rain rate, hence of to provide real-time precipitation maps on wide areas. In fact, though the model was developed using data collected by a custom satellite beacon receiver, the power received by very small aperture terminals (VSATs) and direct to home (DTH) terminals would be the key information to retrieve the rain rate by means of the proposed methodology. The only major limitation could come from a limited dynamic range of the equipment, but this aspect is very peculiar to each single receiver. Another research path to be investigated consists in assessing whether the prediction capabilities can be improved by integrating measurements coming from different domains (e.g., temperature, pressure, humidity, etc.).

ACKNOWLEDGMENT

The authors would like to thank NASA for making available the experimental data within the collaboration with Politecnico di Milano on the Alphasat Aldo Paraboni propagation experiment and ECMWF for the ERA5 dataset.

REFERENCES

- [1] D. Venugopal, C. Muthugadahalli, K. S. Mohanavelu, and K. Narayanan, “Ka band satellite communication systems—Applications and configurations,” in *Proc. Int. Astron. Congr. (IAC)*, Jerusalem, Israel, 2015, pp. 12–16.
- [2] O. Kodheli *et al.*, “Satellite communications in the new space era: A survey and future challenges,” 2020, *arXiv:2002.08811*.
- [3] R. K. Crane, *Electromagnetic Wave Propagation Through Rain*. Hoboken, NJ, USA: Wiley, 1996.
- [4] R. K. Crane, *Propagation Handbook for Wireless Communication System Design*. Boca Raton, FL, USA: CRC Press, 2003.
- [5] J. Louis and J. Ippolito, *Satellite Communications Systems Engineering*. Hoboken, NJ, USA: Wiley, 2008.
- [6] M. Takahashi, Y. Kawamoto, N. Kato, A. Miura, and M. Toyoshima, “Adaptive power resource allocation with multi-beam directivity control in high-throughput satellite communication systems,” *IEEE Wireless Commun. Lett.*, vol. 8, no. 4, pp. 1248–1251, Aug. 2019.
- [7] F. Giannetti and R. Reggiannini, “Opportunistic rain rate estimation from measurements of satellite downlink attenuation: A survey,” *Sensors*, vol. 21, no. 17, p. 5872, Aug. 2021.
- [8] R. A. Giro, L. Luini, and C. G. Riva, “Rainfall estimation from tropospheric attenuation affecting satellite links,” *Information*, vol. 11, no. 1, p. 11, Dec. 2019.
- [9] J. M. Riera, A. Benarroch, P. Garcia-del-Pino, and S. Pérez-Peña, “Preprocessing and assessment of rain drop size distributions measured with a K-band Doppler radar and an optical disdrometer,” *IEEE Trans. Instrum. Meas.*, vol. 70, pp. 1–8, 2021.
- [10] B. Denby *et al.*, “Combining signal processing and machine learning techniques for real time measurement of raindrops,” *IEEE Trans. Instrum. Meas.*, vol. 50, no. 6, pp. 1717–1724, Dec. 2001.
- [11] P. Mariño, F. Machado, F. P. Fontan, and S. Otero, “Hybrid distributed instrumentation network for integrating meteorological sensors applied to modeling RF propagation impairments,” *IEEE Trans. Instrum. Meas.*, vol. 57, no. 7, pp. 1410–1421, Jul. 2008.
- [12] M. Xian, X. Liu, M. Yin, K. Song, S. Zhao, and T. Gao, “Rainfall monitoring based on machine learning by earth-space link in the Ku band,” *IEEE J. Sel. Topics Appl. Earth Observ. Remote Sens.*, vol. 13, pp. 3656–3668, 2020.
- [13] A. Gharanjik, M. B. Shankar, F. Zimmer, and B. Ottersten, “Centralized rainfall estimation using carrier to noise of satellite communication links,” *IEEE J. Sel. Area Commun.*, vol. 36, no. 5, pp. 1065–1073, May 2018.
- [14] F. Giannetti, M. Moretti, R. Reggiannini, and A. Vaccaro, “The NEFO-CAST system for detection and estimation of rainfall fields by the opportunistic use of broadcast satellite signals,” *IEEE Aerosp. Electron. Syst. Mag.*, vol. 34, no. 6, pp. 16–27, Jun. 2019.
- [15] Y. Zhao, X. Liu, M. Xian, and T. Gao, “Statistical study of rainfall inversion using the earth-space link at the Ku band: Optimization and validation for 1 year of data,” *IEEE J. Sel. Topics Appl. Earth Observ. Remote Sens.*, vol. 14, pp. 9486–9494, 2021.
- [16] K. V. Mishra, M. R. B. Shankar, and B. Ottersten, “Deep rainrate estimation from highly attenuated downlink signals of ground-based communications satellite terminals,” in *Proc. IEEE Int. Conf. Acoust., Speech Signal Process. (ICASSP)*, Barcelona, Spain, May 2020, pp. 9021–9025.
- [17] T. Rossi *et al.*, “Satellite communication and propagation experiments through the alphasat Q/V band Aldo Paraboni technology demonstration payload,” *IEEE Aerosp. Electron. Syst. Mag.*, vol. 31, no. 3, pp. 18–27, Mar. 2016.
- [18] J. J. Rivera *et al.*, “Alphasat Aldo Paraboni, an advanced Q/V band mission space segment,” *Int. J. Satell. Commun. Netw.*, vol. 37, no. 5, pp. 397–409, Sep. 2019.
- [19] M. Zemba, J. Nessel, J. Houts, L. Luini, and C. Riva, “Statistical analysis of instantaneous frequency scaling factor as derived from optical disdrometer measurements at K/Q bands,” in *Proc. 10th Eur. Conf. Antennas Propag. (EuCAP)*, Apr. 2016, pp. 1–5.
- [20] J. Miguel Garcia-Rubia, J. M. Riera, P. Garcia-del-Pino, and A. Benarroch, “Propagation in the Ka band: Experimental characterization for satellite applications,” *IEEE Antennas Propag. Mag.*, vol. 53, no. 2, pp. 65–76, Apr. 2011.
- [21] X. Boulanger, B. Benamar, and L. Castanet, “Propagation experiment at Ka-band in French guiana: First year of measurements,” *IEEE Antennas Wireless Propag. Lett.*, vol. 18, no. 2, pp. 241–244, Feb. 2019.
- [22] ITU-R, *Prediction Method of Fade Dynamics on Earth-Space Paths*, document International Telecommunication Union, Geneva, Switzerland, 2005.
- [23] P. Geurts, D. Ernst, and L. Wehenkel, “Extremely randomized trees,” *Mach. Learn.*, vol. 63, no. 1, pp. 3–42, Mar. 2006.
- [24] J. R. Quinlan, “Induction of decision trees,” *Mach. Learn.*, vol. 1, no. 1, pp. 81–106, 1986.
- [25] T. G. Dietterich and K. E. Bae, “Machine learning bias, statistical bias, and statistical variance of decision tree algorithms,” Dept. Comput. Sci., Oregon State Univ., Corvallis, OR, USA, Tech. Rep., 1995.
- [26] G. Louppe, “Understanding random forests: From theory to practice,” 2014, *arXiv:1407.7502*.
- [27] B. H. Menze *et al.*, “A comparison of random forest and its Gini importance with standard chemometric methods for the feature selection and classification of spectral data,” *BMC Bioinf.*, vol. 10, no. 1, p. 213, Jul. 2009.
- [28] ITU-R, *Propagation Data and Prediction Methods Required for the Design of Earth-Space Telecommunication Systems*, document International Telecommunication Union, Geneva, Switzerland, 2017.
- [29] J. Davis and M. Goadrich, “The relationship between Precision-Recall and ROC curves,” in *Proc. 23rd Int. Conf. Mach. Learn. (ICML)*, New York, NY, USA, 2006, pp. 233–240.
- [30] G. Cyril and E. Gaussier, “A probabilistic interpretation of precision, recall and F-score, with implication for evaluation,” in *Proc. Eur. Conf. Inf. Retr.*, 2005, pp. 345–359.
- [31] G. Rätsch, T. Onoda, and K.-R. Müller, “Soft margins for AdaBoost,” *Mach. Learn.*, vol. 42, no. 3, pp. 287–320, 2001.

- [32] Z. Zhongheng, "Introduction to machine learning: K-nearest neighbors," *Ann. Transl. Med.*, vol. 4, no. 11, p. 218, 2016.
- [33] S. Bose, A. Pal, R. SahaRay, and J. Nayak, "Generalized quadratic discriminant analysis," *Pattern Recognit.*, vol. 48, no. 8, pp. 2676–2684, Aug. 2015.
- [34] W. S. Noble, "What is a support vector machine?" *Nature Biotechnol.*, vol. 24, no. 12, pp. 1565–1567, 2006.
- [35] F. Giannetti *et al.*, "Real-time rain rate evaluation via satellite downlink signal attenuation measurement," *Sensors*, vol. 17, no. 8, p. 1864, Aug. 2017.
- [36] C. Mugnai, F. Sermi, F. Cuccoli, and L. Facheris, "Rainfall estimation with a commercial tool for satellite internet in Ka band: Model evolution and results," in *Proc. IEEE Int. Geosci. Remote Sens. Symp. (IGARSS)*, Milan, Italy, Jul. 2015, pp. 890–893.



Riccardo Angelo Giro was born in 1994. He received the M.Sc. degree (*cum laude*) in telecommunications engineering from the Politecnico di Milao, Milan, Italy, in 2019, where he is currently pursuing the Ph.D. degree in information technology.

His main research interests include applied machine learning and deep learning, surveillance techniques for monitoring of oil and gas pipelines, remote sensing, and geophysics.



Lorenzo Luini (Senior Member, IEEE) was born in Italy, in 1979. He received the Laurea degree (*cum laude*) in telecommunication engineering and the Ph.D. degree (*cum laude*) in information technology from the Politecnico di Milano, Milan, Italy, in 2004 and 2009, respectively.

He is currently an Associate Professor at Dipartimento di Elettronica, Informazione e Bioingegneria (DEIB), Politecnico di Milano. He also worked as a System Engineer with the Industrial Unit – Global Navigation Satellite System (GNSS) Department, Thales Alenia Space Italia S.p.A., Rome, Italy. He has been involved in several European Cooperation in Science and Technology (COST) projects, in the European Satellite Network of Excellence (SatNEx), as well as in several projects commissioned to the research group by the European Space Agency (ESA), the USA Air Force Laboratory (AFRL), and the European Commission (H2020). He has authored almost 200 contributions to international conferences and scientific journals. His research activities are focused on electromagnetic wave propagation through the atmosphere, both at radio and optical frequencies.

Dr. Luini is a member of the Italian Society of Electromagnetism, the Board Member of the working group "Propagation" of European Association on Antennas and Propagation (EurAAP), and the Leader of Working Group "Propagation data calibration" within the AlphaSat Aldo Paraboni propagation Experimenters (ASAPE) group. He is Associate Editor of *International Journal on Antennas and Propagation (IJAP)*.



Carlo Giuseppe Riva (Senior Member, IEEE) was born in 1965. He received the Laurea degree in electronic engineering and the Ph.D. degree in electronic and communication engineering from the Politecnico di Milano, Milan, Italy, in 1990 and 1995, respectively.

In 1999, he joined the Dipartimento di Elettronica, Informazione e Bioingegneria, Politecnico di Milan, where he has been a Full Professor of electromagnetic fields, since 2020. He participated in the Olympus, Italsat, and (the running) Alphasat Aldo Paraboni (for this experiment, he has been appointed Principal Investigator by ASI in 2012) propagation measurement campaigns, in the COST255, COST280, and COSTIC0802 international projects on propagation and telecommunications and in the Satellite Communications Network of Excellence (SatNEx). He is the author of about 250 papers published in international journals or international conference proceedings. His main research activities are in the field of the tropospheric effects in satellite microwave links (geostationary Earth orbit (GEO), medium Earth orbit (MEO), low Earth orbit (LEO), and Deep Space) and their statistical and physical modeling, the propagation impairment mitigation techniques, and satellite communication adaptive systems.

Dr. Riva is the Chairperson of WP 3J of International Telecommunication Union–Radiocommunication Sector (ITU-R) SG3 ("Propagation fundamentals") and Associate Editor of IEEE TRANSACTIONS ON ANTENNAS AND PROPAGATION.



Domingo Pimienta-del-Valle was born in Pinar del Río, Cuba, in 1986. He received the bachelor's degree in telecommunication and electronic engineering from the Universidad de Pinar del Río, Pinar del Río, in 2010, the M.S. degree in telecommunication and telematics from CUJAE, La Habana, Cuba, in 2013, and the Ph.D. degree (*cum laude*) in communication technologies and systems from the Universidad Politécnica de Madrid (UPM), Madrid, Spain, in 2019.

Since 2016, he has been working as Research Assistant with the Research Group on Information and Communication Technologies-Radiocommunications, UPM. He has participated in several national and European projects and published several articles and conference papers related with the previous topics. His research interests are focused on satellite and 5G and beyond millimeter-wave propagation and technologies.



José Manuel Riera Salis (Senior Member, IEEE) was born in Avilés, Spain, in 1963. He received the M.S. and Ph.D. degrees in telecommunication engineering from the Universidad Politécnica de Madrid (UPM), Madrid, Spain, in 1987 and 1991, respectively.

Since September 2017, he is a Professor of radio communications at UPM, where he has been an Associate Professor, since 1993. He is currently the Leader of the UPM Research Group on Information and Communication Technologies (GTIC), which is one of the founding groups of the recently established Information Processing and Telecommunications Center (IPTC). He has been the Academic Secretary of the Departamento de Señales, Sistemas y Radiocomunicaciones (1998–2007) and the Vice-Dean for Economic Affairs of the Escuela Técnica Superior de Ingenieros de Telecomunicación (2007–2013). He has been the Leader of nearly 50 research projects, funded by private companies, public agencies or national, and international research programs, including Comisión Europea (CE), European Space Agency (ESA), and European Cooperation in Science and Technology (COST). His Group contributes regularly to the Working Parties of International Telecommunication Union–Radiocommunication Sector (ITU-R) Study Group 3 (Propagation). He is the author of more than 200 technical articles, more than 130 of them published in international journals (40), conference proceedings, or as book chapters. His research interests are in the areas of radiowave propagation and wireless communication systems.

Prof. Salis is an Associate Editor of IEEE TRANSACTIONS ON ANTENNAS AND PROPAGATION.